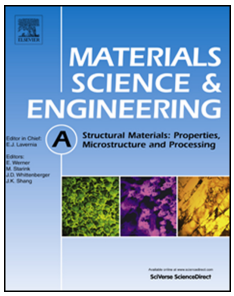
Journal Pre-proof



Analysis of fracture toughness properties of wire + arc additive manufactured high strength low alloy structural steel components

Philip Dirisu, Supriyo Ganguly, Ali Mehmanparast, Filomeno Martina, Stewart Williams

PII: S0921-5093(19)31071-8

DOI: https://doi.org/10.1016/j.msea.2019.138285

Reference: MSA 138285

To appear in: *Materials Science & Engineering A*

Received Date: 13 June 2019

Revised Date: 7 August 2019

Accepted Date: 13 August 2019

Please cite this article as: P. Dirisu, S. Ganguly, A. Mehmanparast, F. Martina, S. Williams, Analysis of fracture toughness properties of wire + arc additive manufactured high strength low alloy structural steel components, *Materials Science & Engineering A* (2019), doi: https://doi.org/10.1016/j.msea.2019.138285.

This is a PDF file of an article that has undergone enhancements after acceptance, such as the addition of a cover page and metadata, and formatting for readability, but it is not yet the definitive version of record. This version will undergo additional copyediting, typesetting and review before it is published in its final form, but we are providing this version to give early visibility of the article. Please note that, during the production process, errors may be discovered which could affect the content, and all legal disclaimers that apply to the journal pertain.

© 2019 Published by Elsevier B.V.

Materials Science and Engineering: A, Volume 765, September 2019, Article number 138285
DOI:10.1016/j.msea.2019.138285

Journal Pre-proof

Analysis of fracture toughness properties of wire + arc additive manufactured high strength low alloy structural steel components

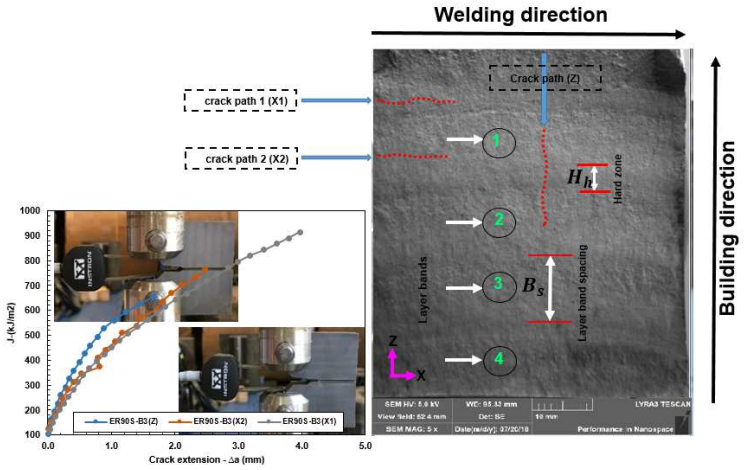
Philip Dirisu [1]*, Supriyo Ganguly[1], Ali Mehmanparast[2] , Filomeno Martina[1] , Stewart Williams[1,]

[1]Welding Engineering and Laser Processing Centre, Cranfield University, Cranfield, MK43 0AL, UK.

[2] Offshore Renewable Energy Engineering Centre, Cranfield University, Cranfield, MK43 0AL, UK.

***Correspondence: taiye.p.dirisu@cranfield.ac.uk; Tel.: +44-777-6644-897

Graphical Abstract: Anisotropic dependence of fracture resistance of cold metal transfer wire + arc additive manufactured (CMT-WAAM) structural steel components of high strength low alloy (HSLA) steel.



Abstract: The uncertainty surrounding the fracture behaviour of CMT-WAAM deposited steel, in terms of crack tip condition (J and CTOD) needed to cause crack tip extension, has made this manufacturing techniques unpopular to date. Fracture toughness parameters are crucial in the structural integrity assessment of components and structures in various industries for assessing the suitability of a manufacturing process and material. In the offshore wind industry, the EN-GJS-400-18-LT ductile cast grade for the mainframe and hub has lower fracture toughness resistance for its high strength grade. Its high weight level affects the Eigen frequency of the tower and imposes high installation cost incurred from heavy lifting equipment usage. Poor fracture toughness is currently a challenge for wind turbine manufacturers owing to the quest for a cleaner and cheaper energy in the offshore wind sector. In this study, CMT-WAAM is used in depositing steel components

Published by Elsevier. This is the Author Accepted Manuscript issued with: Creative Commons Attribution Non-Commercial No Derivatives License (CC:BY:NC:ND 4.0).
The final published version (version of record) is available online at DOI:10.1016/j.msea.2019.138285. Please refer to any applicable publisher terms of use.

Journal Pre-proof

with an oscillatory and single pass deposition strategy. The effects are shown of how the microstructural variation, as a result of layer by layer deposition and the layer band spacing, affects the fracture resistance in the build and welding direction. The fracture mechanics and failure mode of the WAAM deposited parts are investigated. The microstructural variation, again as a result of the layer by layer deposition and the layer band spacing, are the key parameters that control the fracture toughness of WAAM steel. Anisotropic behaviour in the J_q values is discovered in both fracture orientations. The constructive transformation mechanism of the WAAM oscillatory process made way for intragranular nucleation of acicular ferrite on the Ti containing inclusion, thereby improving the toughness of the ER70S-6 deposit with a unique microstructure and J_q value of 640KJ/m^2 .

Keywords: High strength low alloy steel (HSLA); CMT wire + arc additive manufacturing (CMT-WAAM); J_{IC} fracture toughness; layer band spacing; microstructural variation.

1. Introduction

The pursuit for cleaner energy generation and the vast availability of wind energy offshore has called for the need to improve the structural materials currently being used and the manufacturing process [1]. Wind power is currently the world's fastest growing source of energy. Owing to the current trend for the quest for renewable wind energy by the UK government, a target was set for Vision 2020 [2]. A typical wind turbine is comprised of 10-25 tons of ductile grade EN-GJS-400-18-LT. This ductile cast grade is used for casting the rotor, hub and mainframe before machining [3,4]. The key issue with the casting process is the endangering of the environment by its high carbon footprint coupled with its high cost involvement. The second key issues are associated with the material's response; high strength ductile cast grades respond poorly to fracture resistance, in addition to their high weight level, which affects the Eigen frequency of the turbine. This is likely to limit its application in larger wind turbines as more exploration of wind offshore is imminent. In order to build larger and lighter wind turbines to be used in deep waters, lighter materials with enhanced fracture toughness and strength properties will be needed.

The use of modern high strength low alloy (HSLA) steel for the wind industry will allow for the reduction in weight and cost of some specially made components [5]. The cost saving from installation and reduced

Journal Pre-proof

inspection times as a result of damage tolerance material (HSLA steels) usage is enormous. HSLA steels micro-alloyed with Ti, V, Nb and Al, in addition to the low carbon content, increase strength and toughness through the various steel strengthening mechanisms [6]. Other elements such as Mo and Cr are useful in promoting bainite formation while Mn and Ni increase the hardenability of the weld metal by helping in the formation of more acicular ferrite, and Ni on its own helps in solid solution strengthening. The volume fraction of any of this microstructure, i.e. acicular ferrite, granular bainite, polygonal ferrite, pearlite, and martensite, form in the microstructure of HSLA steel depending on the proportion of alloying element composition, and deposition parameters used [7,8]. In all these structures, acicular ferrite is the most preferred because of its fine non-equiaxed interlocking basket weave features and its fine grain size that promotes maximum resistance to crack growth propagation and superior fracture toughness properties [9]. The influence of acicular ferrite formation is felt in low carbon alloyed steel; it also has good strength and fracture toughness. Lower C content in bainitic steel eliminates the inter lath cementite (martensitic formation) and improves the fracture toughness of bainitic steel [10–12], but is still inferior to the fracture toughness of high acicular content steels [13]. It has been proven that increased cooling rate with a high volume fraction of TiO_2 inclusion within the austenite enhances the formation of acicular ferrite in low carbon low alloy steel deposition [14,15]. Most of the current filler wires are designed to benefit from this known fact about acicular ferrite formation [16]. The fine carbonitride particles and the martensite/austenite laths present in acicular ferrite give the structure the desired strength effects [17,18].

The use of CMT-WAAM is a reliable design option to produce bespoke components for the renewable energy industry due to its cost savings advantage and design flexibility using specially tailored wires (raw feed) with potential for acicular ferrite formation. This technique is initially predominant in the aerospace industry but has recently become a subject of interest in other energy sectors, such as the renewable energy industry. The unique WAAM process, which entails the controlled deposition and bi-directional oscillatory and single pass strategy, is a plus to the manufacturing technique. The WAAM option will enable the production of larger, lighter wind turbine components using an alternative source of materials that are lighter and have excellent fracture toughness properties. The microstructural features in WAAM are composed of layer bands and microsegregation distributed along the build direction as a result of the repeated thermal cycling suffered by the material; these layer bands are sometimes representative of the layer height. The inherent low angle grain boundaries resulting from the re-melting line results in dendritic grain growth in the build direction [19,20]. The

Journal Pre-proof

dendritic structures are sites prone to microsegregation and compositional inhomogeneity, hence the non-uniformity of the mechanical properties [21]. In the Ti64 WAAM deposited part, a weak microsegregation at the fusion boundary of each remelt layer was discovered as a result of the solute boundary layer developed at the solidification front. These fusion boundary segregations reduce the stability of the ß phase, thereby forming coarse columnar grains with a strong texture that leads to anisotropy in properties; it was clear from this study that layer bands spacing and the extent of re-melting from each deposited layer could be responsible for the mechanical behaviour of a WAAM component [22].

Haden et al. found no significant anisotropy in the mechanical properties of ER70S-6 deposited with WAAM, although the part thickness was 6.53 mm [23]. Rodrigues et al. revealed that the microstructural features obtained with WAAM deposited HSLA steel were ferrite, bainite, and M-A, with uniform mechanical properties and texture in both longitudinal and normal directions, although the part deposited thickness was between 8.2 - 9.4 mm [24], The results were similar to those of Haden et al. Rodrigues et al. single pass wall was built with a low heat input. However, this microstructural uniformity might not be the case when high heat input and high thickness with a different deposition strategy are deployed. Sridharan et al. discovered that high heat input and slow cooling rate achieved when ($\Delta t_{8/5}$) > 30 seconds is required for building WAAM structures with less anisotropy in mechanical properties [14], They further stated that properties in the Z-direction give a better impact toughness strength, although there was variation in the thickness deposited in the X, Y & Z directions tested.

Linear-elastic fracture mechanics (LEFM) according to ASTM E399 is used extensively for high strength metallic materials with many restrictions on the minimum size of the specimen that can be tested [25]. Fracture mechanics specimens with sufficiently large thickness are required for a valid K_{IC} test under small scale yielding and plane strain conditions. This is practically impossible with WAAM technology as a result of non-uniformity in the microstructure. The plastic zone at the crack tip is proportional to the ratio of $\left({K_{IC}}^2 \middle| Ys^2\right)$ and will only have a negligible effect on the stress around the crack and the measured K_{IC} value when the specimen dimension a, b, B $\geq$ $2.5\left({K_{IC}}^2 \middle| Ys^2\right)$ [26]. An alternative method is to use the J_{IC} test method in accordance with ASTM E1820 based on elastic-plastic fracture mechanics (EPFM), which gives room for the use of smaller compact tension C(T) specimen geometry.

Regardless of the efforts made to characterize the wire + arc additive manufactured structural steel components, all current research focuses on single pass WAAM deposited steel components with a thickness not exceeding

Journal Pre-proof

10 mm; most of the research only focuses on microstructural properties and mechanical strength, but none on fracture toughness. Moreover, previous studies on HSLA steel welding do not represent the actual thermal conditions inherent in WAAM. In this research, detailed analysis of the fracture toughness properties of oscillated CMT-WAAM steel components was carried out to understand how the microstructural variation, as a result of the layer band, affects the fracture resistance in the build and welding direction. This investigation also points out the fracture mechanics and failure mode of the WAAM oscillated steel structure.

2. Materials and methods

2.1 WAAM process description and sample preparation

The CMT-WAAM of the structures was carried out using the standard cold metal transfer welding process, which is a modified gas metal arc welding process based on a controlled dip transfer mode mechanism [27]. A Fronius CMT (VR 7000 CMT) power source with a wire feeder and a CMT torch connected to an IRB 2400 ABB robot was used, as shown in Fig. 1 (c). Local shielding was done with spec shield light (80%Ar + 20%CO_2) for ER70S-6 and ER120S-G and spec shield heavy (Ar +2%O_2) for ER90S-B3 at a flow rate of 15L/min. The base plates used in the experiment are rolled structural steel plates of S275 JR (EN10025) with dimensions of 250 mm x 200 mm x 15 mm. The plates were clamped by a steel jig tightened to an aluminum base plate. The wire diameter used was 1.2 mm. The deposition was done in the PA (1G/Down hand) position from the base of the plate with the torch and wire feeding in the vertical direction. BÒHLER ER120S-G and ER90S-B3 with Lincoln ER70S-6, as shown in Table 1, were used.

The oscillatory pass (OS) and single pass (SP) strategies, as shown in Fig. 1 (a & b), were used to deposit layer by layer onto the substrate with the bi-directional movement of the torch. A portable arc monitor was used to monitor the weld parameters. The following weld parameters were recorded: current, 157 amps; voltage, 13.3 volts; heat input, 0.313 kJ/mm; WFS, 6.5 m/min; TS, 0.4 m/min; CTWD, 11.5 mm; and dwell time, 60 secs. For each successive layer deposition, a layer height increment of 3.5 and 1.7mm of the torch distance from the previously deposited layer was targeted for the oscillatory and single pass. For the oscillatory strategy, two walls each were built with the wires, totalling six walls for the three different grades studied, with a dimension of 290 mm x 120 mm x 24.5 mm. One wall each was built for the single pass strategy as shown in Fig. 2 (a).

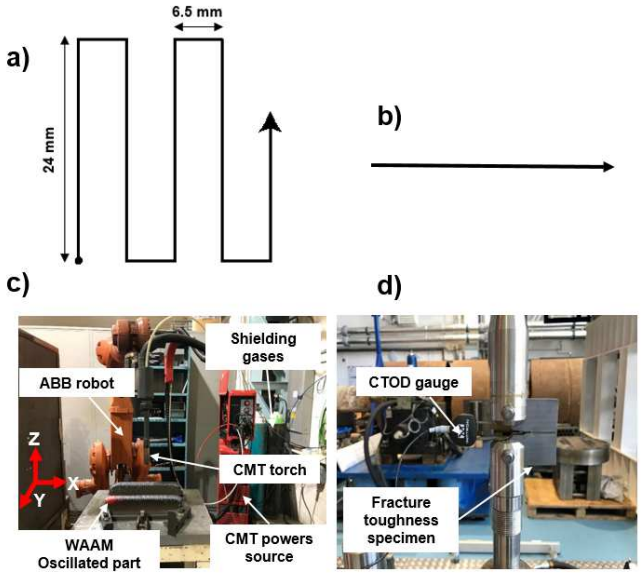


Fig. 1. (a) WAAM oscillatory pass strategy (b) Single pass strategy (c) WAAM built (d) J_{IC} fracture toughness testing

Table 1. Chemical Composition (%wt) of Wires

Alloys	C	Si	Mn	P	S	Cr	Mo	Ni	V	Cu	Nb	Ti	Al	Zr
ER70S-6	0.06	0.940	1.640	0.013	0.016	0.020	0.005	0.020		0.020		0.004		0.002
ER90S-B3	0.08	0.58	0.89	0.005	0.002	2.4	0.99	<0.1	<0.01	<0.1	<0.01			
ER120S-G	0.10	0.79	1.77	0.008	0.010	0.35	0.63	2.27	<0.01	0.07		0.07	<0.01	<0.01

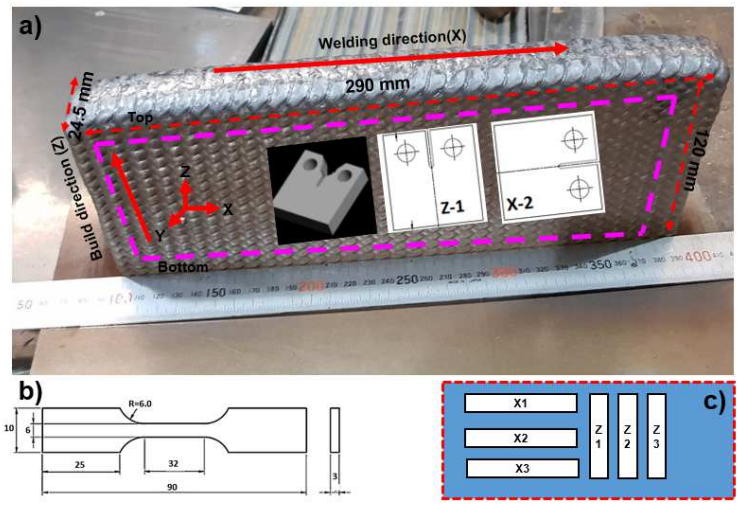


Fig. 2. (a) Oscillatory deposited wall geometry with C(T) machining matrix (b) tensile cut specimen (c) tensile specimens' machining matrix

2.2 Mechanical and microstructural characterization method

Eighteen tensile specimens (six from each grade), as shown in Fig. 2 (c), were cut from both the oscillatory and single pass built wall in both the build and welding directions; all specimens were prepared following ASTM E8/E8M-16a. The uni-axial tensile testing was performed with an electromechanical controlled instron 5500R machine with a load cell of 30 kN using a strain rate of 1mm/min. The metallography samples were extracted from the as-deposited (AD) walls and prepared with a Buehler Metaserve 250 grinder and polisher machine before the micro-examination and Vickers hardness testing. The ground and polished samples were etched in 2% Nital (Ethanol and Nitric acid) to reveal the microstructure at various magnifications using an optical microscope (Meiji Japan). A scanning Electron Microscope (SEM, FEI XL 30-SFEG) equipped with energy dispersive spectrometry (EDS) detector was used to characterize the fracture toughness surfaces and elemental composition of inclusions and carbides in the WAAM deposit. The Vickers hardness testing was done at room temperature using the Zwick/Roell hardness testing machine. An average of 42 idents was made on the polished surface along the build direction using a 300 g load at a spacing of 0.5 mm.

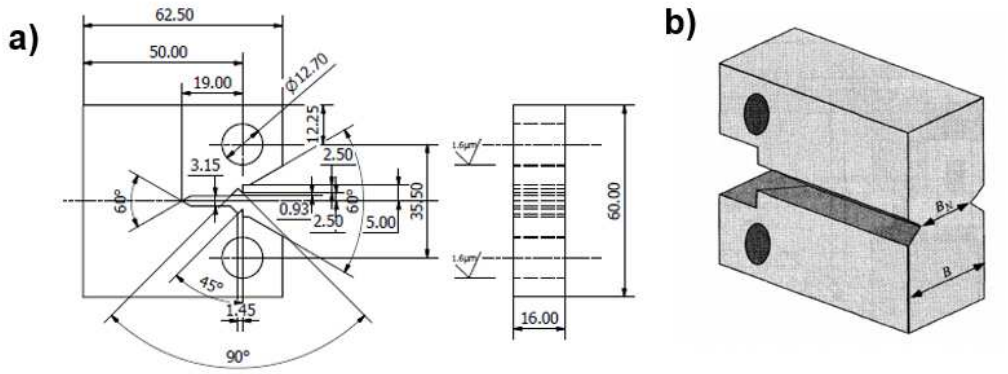


Fig. 3. (a) C(T) specimen dimensioned as per ASTM E1820 (b) side grooved C(T) specimen geometry

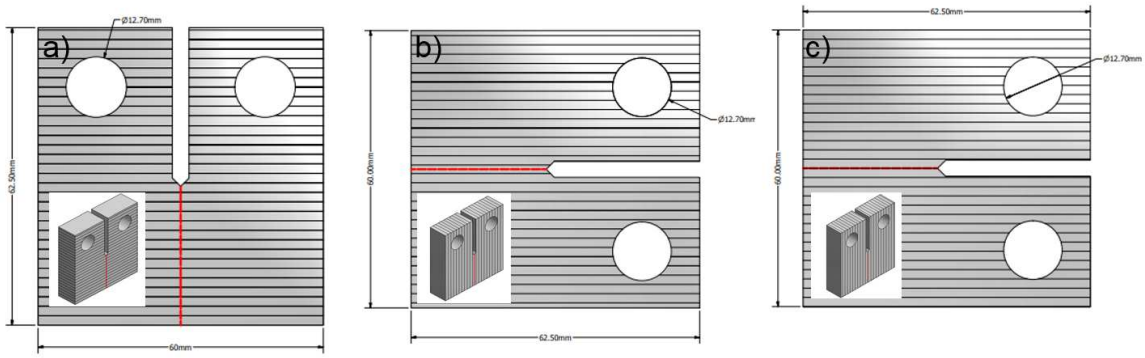


Fig. 4. J_{IC} Fracture testing (a) across the layers (Z-direction sample) (b) along the layers (X-direction sample (X2)) (c) along the layers (X-direction sample (X1))

2.3 Fracture toughness characterization method

The oscillatory build walls with a thickness of 24.5 mm were machined, as shown in Fig. 2 (a). The C(T) specimens were cut and machined from two different orientations of the deposited structure. The first orientation was from the Z-direction (grooved notch perpendicular to the layer band and welding direction), as shown in Fig. 4 (a). The groove notch was placed in two different locations on the second orientation (grooved notch parallel to the layer bands and welding direction). In the first location, the grooved notch was in between two layer bands, as shown in Fig. 4 (b) and in the second location, the grooved notch was placed on the layer band boundary, as shown in Fig. 4 (c). Three C (T) specimens, each of dimensions 60 mm x 62.5 mm x 16 mm, were prepared from each grade according to the ASTM E1820 standard using electronic discharge machining (EDM), as shown in Fig. 3 (a). Fatigue pre-cracking and fracture toughness test as per J-integral was conducted with an instron 8801 servo-hydraulic machine with a load cell of 100kN. An initial crack starter of ($\boldsymbol{a_o}$ = 19mm) was machined by EDM. The fatigue pre-cracking was done with a frequency of 5Hz to attain a fatigue crack size range (total average length of the crack starter configuration + fatigue crack) of 0.45W - 0.70W using the K- decreasing approach with the maximum stress intensity in the first step limited to $\boldsymbol{K_{max} = (\sigma^f Ys | \sigma^T Ys)(0.063 \sigma^f Ys MPa\sqrt{m})}$, where $\boldsymbol{\sigma^f Ys}$ & $\boldsymbol{\sigma^T Ys}$ are the material yield stresses at fatigue pre-crack and test temperature. This was done to introduce a sharp crack tip without allowing a significant plastic zone to develop ahead of the starter crack tip. The pre-cracked C (T) samples were latter side grooved to 0.2B, where B is the final thickness of the C (T) specimen (20% of total thickness) on both faces of the sample along the pre-cracked path to further introduce a dominant plane constraint to minimize plastic zone formation, as shown in Fig. 3(b). All specimens had width, total thickness and net thickness of W, 50 mm; B, 16 mm; and $\boldsymbol{B_n}$, 12.8 mm, respectively. The fracture toughness test was performed by applying sequences of loading and partial unloading at specified intervals. The load and load line displacement (LLD) data were measured

Journal Pre-proof

using a clip gauge attached to the crack mouth of the C(T) specimen. The test was performed under LLD control mode with 5-minutes holding time, followed by 20% unloading at each peak load. The unloading slopes, which are linear and independent of prior plastic deformation, were used to estimate the instantaneous crack length at each unloading increment using the elastic compliance relationship. All tests were performed at room temperature with a loading and unloading rate of 0.50 mm/min and an LLD increment of 0.125 mm.

2.4 Equations employed in data analysis

The fatigue pre-cracking was done as per ASTM E1820 using a force value based on the force $\boldsymbol{P_m}$

$$\boldsymbol{P_m} = \frac{\mathbf{0.4}\, \boldsymbol{Bbo^2 \sigma_y}}{\mathbf{2w + a_0}} \quad (1)$$

The fracture toughness of ductile material can be characterized using the EPFM parameter J, as per ASTM E1820. J can be divided into an elastic component $\boldsymbol{J_{elastic}}$ and a plastic component $\boldsymbol{J_{plastic}}$

$$\mathrm{J} = J_{el} + J_{pl} \quad (2)$$

$$J_{(i)} = \frac{K_{(i)}{}^2(1-\nu^2)}{E} + \left(\frac{\aleph_{pl} A_{pl}}{B_N b_o}\right) \quad (3)$$

where $J_{(i)}$ is the instantaneous fracture resistance energy, $K_{(i)}$ is the instantaneous stress intensity factor calculated from Eq. (4 & 5) below, E is the Young modulus, ν is the Poisson ratio, B_N is the net specimen thickness between the side grooves, b_o is the uncracked ligament, (W-a_0) and $\aleph_{pl}$ = 2+0.522b_o/W($CT\ specimen$). a_0 is the initial crack length and W is the specimen width. A_{pl} is the plastic area under the load versus displacement curve, as described in ASTM E 1820.

$$K_{(i)} = \frac{P_{(i)}}{\sqrt{B.Bn}.\sqrt{w}}.f(\frac{a}{w}) \text{ (MPa}\sqrt{\text{m}}) \quad (4)$$

$$f(\frac{a_i}{w}) = (2+\frac{ai}{w})\left[0.886 + 4.64\frac{a_i}{w} - 13.32\left(\frac{a_i}{w}\right)^2 + 14.72\left(\frac{a_i}{w}\right)^3 - 5.6\left(\frac{a_i}{w}\right)^4\right] / \left(1-\frac{a_i}{w}\right)^{3/2} \quad (5)$$

The J versus Δa (incremental crack growth), also known as the J-R curve, was generated to find the fracture toughness properties of the WAAM HSLA steel. A blunting line was constructed in the J-R curve using Eq. 6,

Journal Pre-proof

the slope of which was used for the exclusion lines at Δa offset of 0.15 mm, 0.20 mm and Δ_{amax}, which is the maximum allowable crack size in fracture analysis.

$$J = 2\sigma_y \Delta a \text{ Where } \sigma_y = \frac{\sigma_{UTS}+\sigma_y}{2} \quad (6)$$

The fracture toughness testing was done here using a single specimen approach where the specimen is subjected to a sequence of loading and unloading. The instantaneous crack length at each peak load, a_i, was estimated using Eq. 7

$$\frac{a_i}{W} = 1.000196 - 4.06319u + 11.242U^2 - 106.043U^3 + 464.335U^4 - 650.677U^5 \quad (7)$$

Where;

$$U = \frac{1}{\left(B_e EC_{c(i)}\right)^{1/2}+1} \quad (8)$$

In Eq. (8), $C_{c(i)}$ is the load line crack opening elastic compliance and B_e is the specimen effective thickness calculated by

$$B_e = B - (B - B_N)^2 / \mathrm{B} \quad (9)$$

Where B is the specimen thickness

3. Results

3.1 Mechanical properties

The variation in ultimate tensile strength (UTS), yield strength (YS) and percentage elongation (PCE) across the three WAAM steel structures with the different deposition strategies are shown in Fig. 5. The SP strategy, which was deposited with layer by layer single bead molten steel, has one unique TS and cools very fast as a result of more heat conduction routes along the build. Hence its limited deposited thickness, compared to the OS strategy, which has two unique TS. Despite having the same heat input, its advancement speed in the oscillation direction (wider width) makes it retain localised heat accumulation as a result of the torch oscillating at a location for a longer time. This is responsible for the variation in microstructure and mechanical properties. The minimum

UTS and YS of these WAAM deposited structures are comparable to their wrought categories. The SP showed higher UTS and YS with ER120S-G & ER90S-B3 deposit, with average values of 987 MPa and 870 MPa respectively. ER90S-B3 UTS, YS & PCE obtained here were typical of F22 wrought steel. The ER70S-6 in the OS had higher UTS but lower YS and PCE; this is typical of A36 Wrought [28]. It is also worth noting that the mechanical behaviour of WAAM deposit is due to the direction of heat flow, grain growth, layer stacking, and thermal gradient obtained during the deposition process. The Cr, Mo, and Ni in this alloy composition increased the hardenability, giving the high strength non-equilibrium phase martensite and bainite (M&B). The wires used for this experiment have low carbon content for improved weldability, as shown in Table 1. The key influencing factor to the mechanical behaviour of the WAAM deposit is the chemistry of the wires, which gives way for different microstructural formation as a result of the cooling rate imposed by the WAAM OS deposition strategy. A typical comparison of the anisotropic behaviour of the OS WAAM steel deposit is shown in the stress-strain curve presented in Fig. 6. It is clear from the plot that the strength properties of the OS strategy are higher in the Z-direction, but ductility is better in the X-direction.

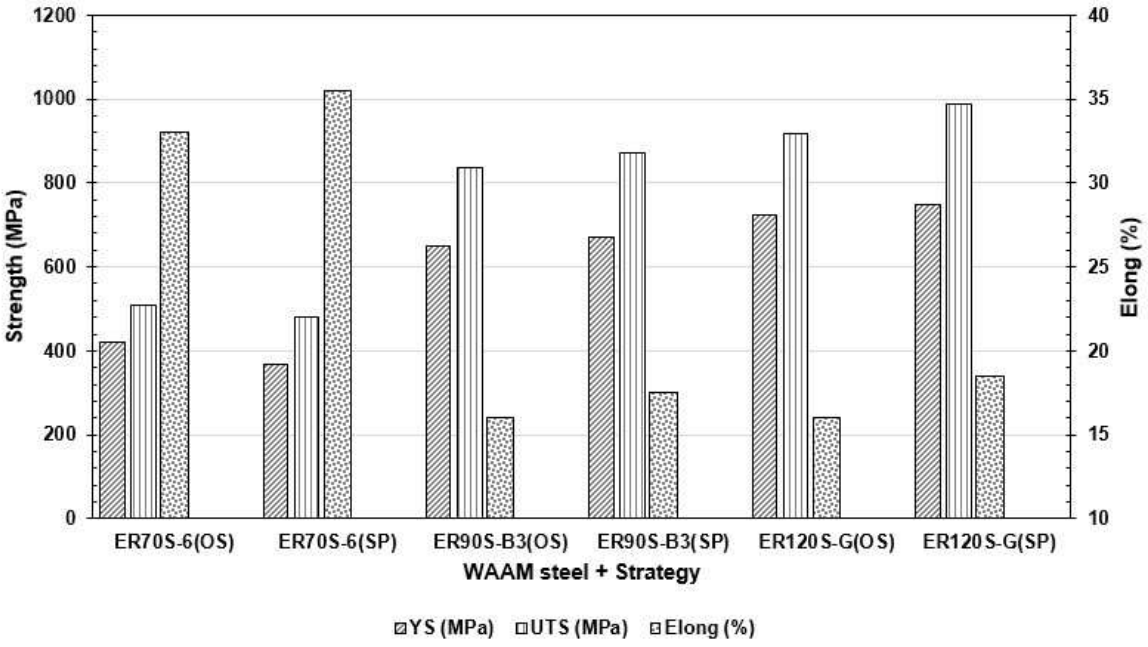


Fig. 5. The average value of strength vs. elongation for both strategies

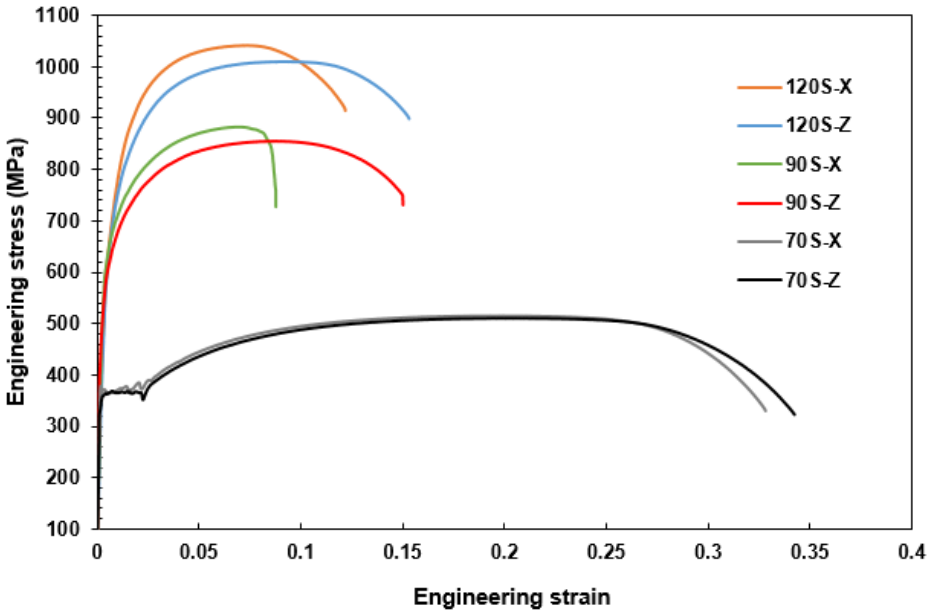


Fig. 6. The stress-strain curve obtained in Oscillatory strategy

3.2 Hardness and microstructure and variation

Fig. 7 presents the hardness variation in the WAAM oscillated structure, while the microstructural variation obtained is shown in Fig. 8. The average hardness obtained for the ER70S-6, ER90S-B3, and ER120S-G is 268HV, 262.3HV, and 326.56 HV, respectively. The prolonged thermal cycle and the increased austenite grain size are responsible for the increases in hardenability in these materials. A similar situation has been reported in [29,30]. The layer stacking and thermal cyclic heating, which cause the hardening and softening of adjacent layers, are responsible for the hardness variation, as seen in Fig. 7; similar hardness trends were reported in the WAAM structure built with HSLA steel and maraging steel [20,24]. The ER120S-G microstructure, as revealed in the SP (Fig. 8 (a)), presents a majorly martensitic lath (ML), quasi polygonal ferrite (QPF) formed as a result of fast cooling while the OS (Fig. 8(d)) contains some martensitic austenite (M-A), acicular ferrite (AF) and intercritical ferrite (IF) formed as a result of the slow cooling rate due to the process. The microstructure of the ER90S-B3 OS, as presented by Fig. 8 (e), is coarser than the SP (Fig. 8 (b)) with some clearly defined prior grain boundaries showing some grain boundary ferrite (GBF) decorated with finely dispersed carbides (Fe_3C +Mo_2C) as a result of cooling rate and prior composition. This is detrimental to fracture toughness, as the structure provides a pathway for crack propagation [31]. The tempered bainite lath (TBL) was formed as a result of the successive softening and hardening of adjacent layers. The microstructure presented by the ER70S-6 SP

(Fig.8(c)) contains majorly of polygonal ferrite (PF) and pearlite (P), while the OS (Fig.8 (f)) is coarser with some PF and a network of basket weave AF nucleated intragranularly from the non-metallic inclusion sites. This basket weave feature has been reported to be a hindrance to crack propagation but supportive of increasing fracture toughness [32].

The grain sizes are larger in the OS than the SP owing to the heat accumulation effects in the OS, which favours grain growth. In both deposition strategies, they are in the increasing order (ER120S-G, ER90S-B3 & ER70S-6). According to the Hall Petch equation relating yield strength and hardness to grain sizes, $\sigma_y = \sigma_o + Kd^{-1/2}$ and $H = H_o + K^1 d^{-1/2}$, where σ_y , H & d are the yield strength, hardness and grain size. σ_o, H_o, K & K^1 are constants independent of grain size. A larger grain size will decrease the mechanical barrier to have a complete martensitic transformation; hence, the reduction of grain size leads to an increase in hardness and yield strength (fine grain strengthening mechanism). The carbide forming elements such as Cr & Mo in the original chemistry result in secondary hardening, which in alliance with the refined dispersion of carbides benefits the toughness. In the case of ER90S-B3, The heat accumulation in the oscillatory strategy lead to the formation of coarse carbides arranged in large lumps, which lower the fracture toughness in the re-melt zone. The precipitates further dissolved back into solid solution with smaller uniform distributed carbides of Mo_2C in the tempered region, thus creating the recrystallised, refine, soft and homogeneous microstructure which aids higher strength and fracture toughness as possessed by the refine zone.

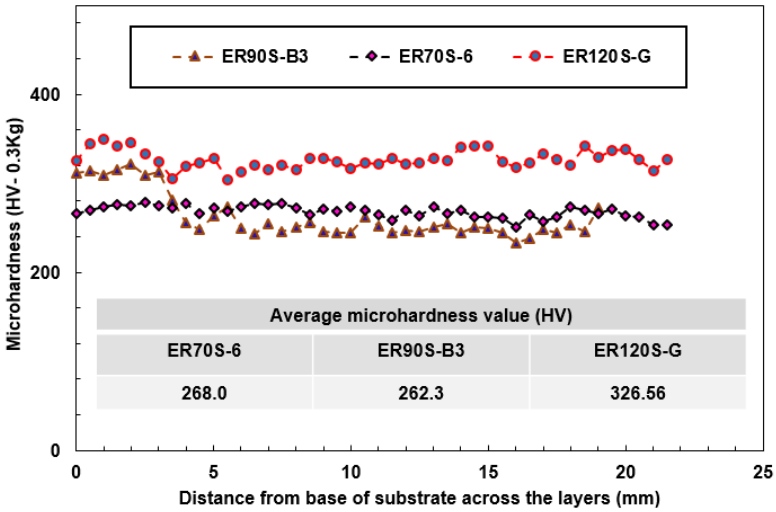


Fig. 7. Hardness variation in WAAM oscillated strategy

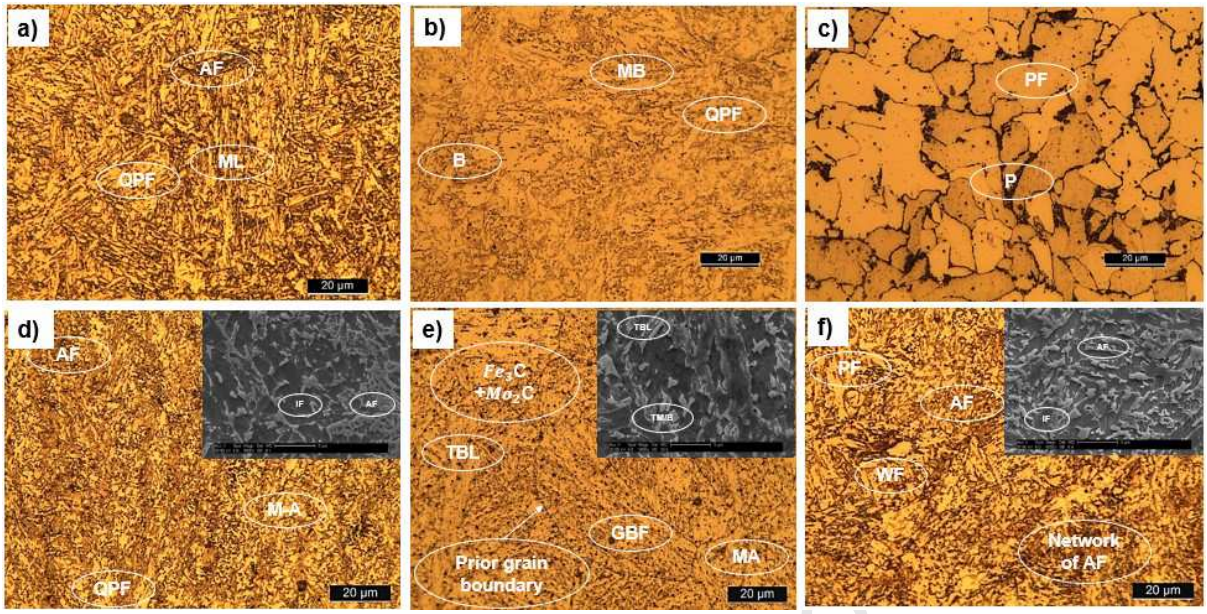


Fig. 8. Optical micrographs of single pass deposition (a) ER120S-G (b) ER90S-B3 (c) ER70S-6, Oscillatory pass deposition with SEM image in picture (d) ER120S-G (e) ER90S-B3 (f) ER70S-6

3.3 Fracture toughness variation (J_{IC})

Fig. 9 presents the loading and unloading LLD and J-R resistance curve based on J-integral. Fig. 10 presents the typical J_{IC} plot with exclusion lines and the J_q values in the different crack orientation for the various WAAM OS deposited steel components. The maximum J_q values, which represent the crack initiation toughness corresponding to the various WAAM deposited steels components, are presented in Table. 2. Fig. 11 presents the macro image showing layer bands and fractured cracked path in the WAAM deposited steel component, as shown in Fig. 4. Fracture in the Z-direction (across the layers) could only occur in crack path Z, while fracture in the X-direction (along the layers) could occur in crack path X1 or X2. The variation in toughness, as given by the J_q values with respect to crack orientation, is evident in the LLD and J-R curves. The observed fracture toughness across the build direction (layer bands) presents the highest resistance to fracture failure, followed by fracture in the welding direction (X-direction). X1 path through the hard zone showed the least toughness. X2 path possessed more resistance to fracture than the X1 path, being the annealed, tempered and refined path. The J-R plots indicated higher resistance to crack propagation in the ER70S-6 WAAM component compared to other WAAM steels, as given in Fig. 10 (b). The J_q values for ER90S-B3 WAAM component were higher in the Z-direction compared to the X-direction, although the highest J_q value for this component is significantly less compared to the ER70S-6 WAAM component. The average J_q values for ER120S-G and ER70S-6 were very

close but significantly higher than the ER90S-B3 WAAM steel. The J_q value for ER120S-G in the Z-direction is about 1.1 & 2.3 times more than the value in X2 and X1 fracture orientation, as reflected in Fig. 10 (b). It is worth noting that the J_q values are generally higher in the Z-direction as the annealed and tempered region of the layer band serves as a ,crack arrest region retarding the fracture; this was also reported with Ti-6Al-4V [33]

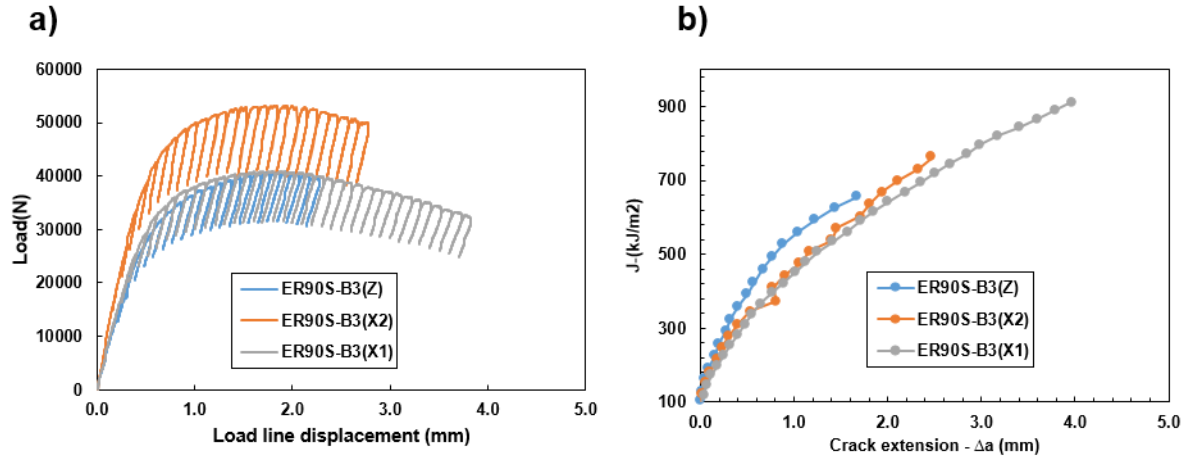


Fig. 9. WAAM deposited structure of (ER90S-B3) (a) loading and unloading curve (b) J-R curves

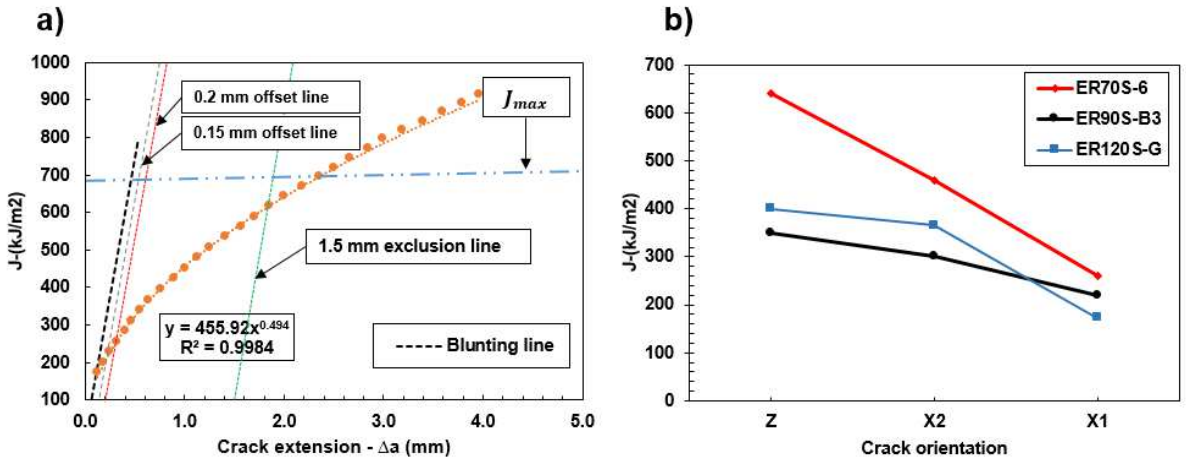


Fig. 10 J_{IC} plot (a) illustration of the exclusion lines, J_{max} and J_{IC} (b) J_q values for the different fracture orientation in WAAM deposited steel components

Table 2. Summary of fracture toughness test results

WAAM steel grade	Max, J_Q(kJ/m2)	Crack orientation	Avg J_Q(kJ/m2)	Max J1c(MPa.m)	dJ/da(MPa)	R^2
120s	400	Z-Dir	313	0.40	978.1	0.99
90s	350	Z-Dir	290	0.35	541.73	0.99
70s	640	Z-Dir	453	0.64	678.47	0.98

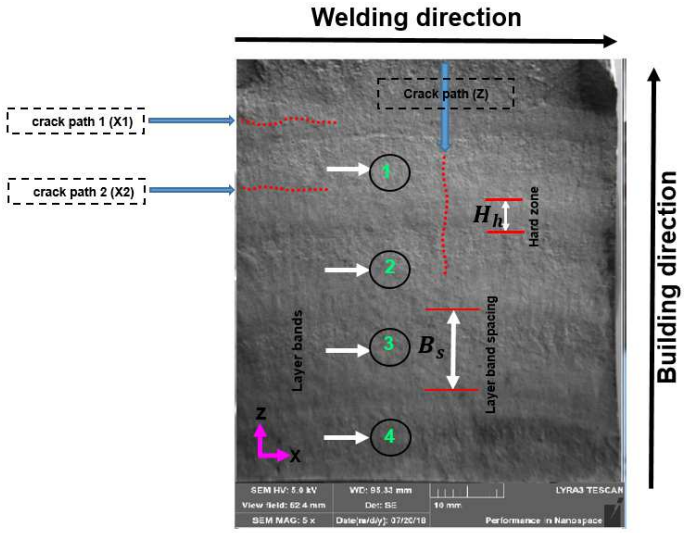


Fig. 11. Macro image showing layer bands and fractured cracked path in WAAM deposited steel component

4. Discussion

4.1 The influence of deposition strategy on microstructure and hardness variation

The cyclic heating of this WAAM steel due to the sequential layering strategy (oscillatory strategy) results in variations in the peak temperature and cooling rates of the adjacent layer in the building direction. The variation in peak temperature, which was as a result of the cooling rate is dependent on the WFS, TS (heat input) and the oscillatory dwell time and leads to the formation of layer bands. These bands have distinctive regions which, on subsequent cyclic heating, cause annealing and softening of the adjacent layers. This phenomenon was also reported for Ti-6Al-4V by [34] and further investigated by [22]. The layer band spacing, which is equivalent to the layer height, causes variability in microstructure and hardness of deposit, as shown in Fig. (7 & 8). This trend is also similar to phase changes in the HAZ of steel welding as observed by [35]. The prolonged thermal cycle in the OS resulted in grain coarsening, which is absent in the SP strategy, as observed in [24] and higher hardness as a result of an increase in austenite grain size, also reported by [29,30] which also increases hardenability. The OS strategy has a feature of increased thermal mass and a slower cooling rate, giving enough time for carbon to diffuse into the austenite.

4.2 The influence of crack orientation on fracture toughness behaviour and mechanism in the Z-direction

The macro of the fractured C (T) specimen, fractured in the Z-direction (across the layers), is presented in Fig. 12 (a - b), while that of the X-direction (along the layers) is presented in Fig. 12 (c - d). The surface revealed

ductile tearing with some resistance across the layer bands in the Z-direction. The layer bands contain some hard and soft zones, as shown in Fig. 11. These two zones represent the peak and valley in the hardness plot shown in Fig. 7. The hard zones are comprised of large grain size of a low proportion of low angle grain boundaries with misorientation angle between 2° and 15° and the soft zones are comprised of small grain size of a high proportion of high angle grain boundaries with misorientation angle greater than 15°. The distance between the two layers (band spacing:B_s) and the height of the coarse grain region (hard zones:H_h), which looks like the HAZ region in an intercritically reheated weld, could be the key to fracture toughness resistance of the WAAM OS steel structures. The soft zones contain a prior austenitic grain boundary, which promotes maximum resistance to crack growth propagation and crack arrest. At the hard zones, just at the re-melting interphase, there is a directional grain growth parallel to the build direction (Z-Dir), being the region most affected by the temperature gradient of the solidifying liquid. This dendritic laths emanating from this liquid-solid interface is also influenced by the composition of the solute [36,37]. Although earlier results on WAAM showed this same trend [38], it is supposed that the soft region will lead to slower crack propagation through the build direction. Crack path roughness is also associated with the fracture in the Z-direction (across the layers), being a tortuous fracture path, as shown in Fig. 12 (a & b). The J_q recorded for the Z-direction were higher than the values recorded for the X-direction. The phenomenon discussed above was responsible for this difference in fracture resistance.

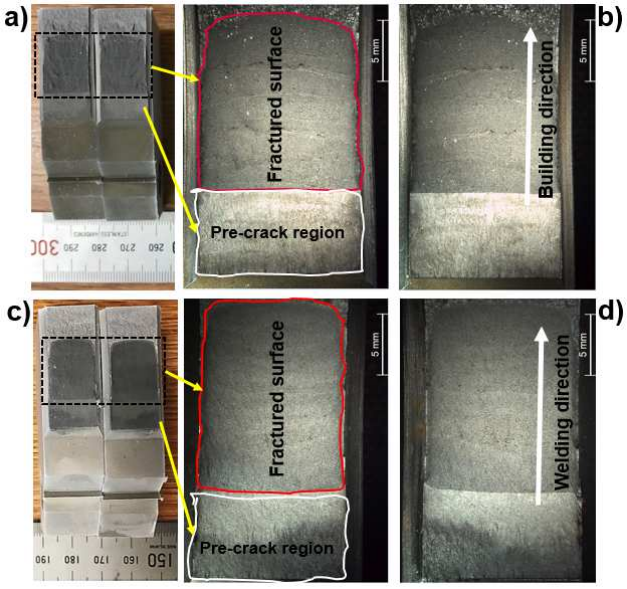


Fig. 12. Macro of fractured C (T) specimen in both directions (a) Z-direction (b) fractured area (c) X-direction. (d) fractured area

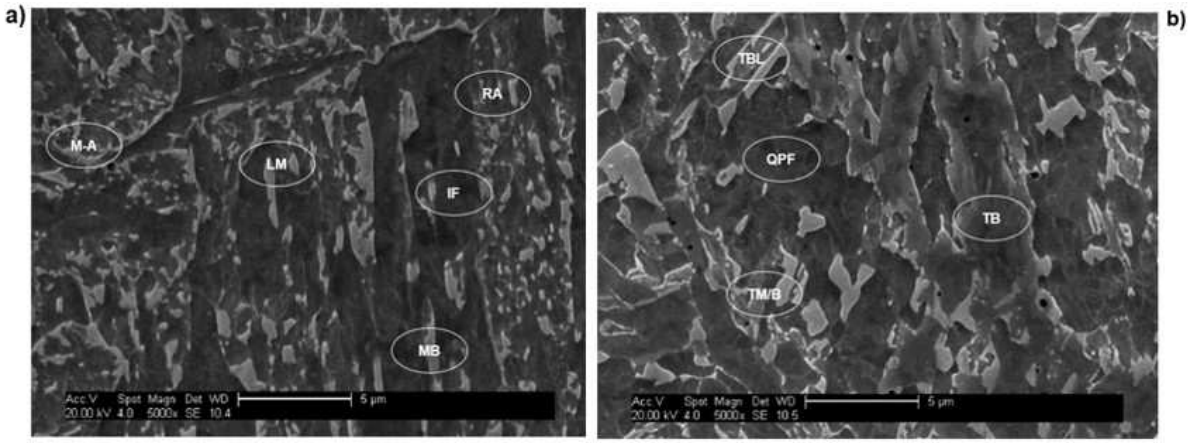


Fig. 13. SEM detailed microstructural features of ER90S-B3 WAAM oscillatory deposited features with fine distribution of carbides (a) X1 fracture path (b) X2 fracture path

4.3 The influence of crack orientation on fracture toughness behaviour and mechanism in the X-direction

SEM details of the WAAM OS microstructural features of 90S-B3 steel obtained in the X1 and X2 paths are shown in Fig. 13. The crack path X2 is the soft region and crack path X1 is the hard microstructural region, as shown in Fig. 11. The fracture C(T) specimen displayed in Fig. 12 (c & d) revealed ductile tearing with less resistance across the path due to the absence of layer bands. The crack path was constrained in these regions by side grooving, as shown in Fig. 3 (b). The path with the least resistance, as shown in the J-R plot, is the X1 path. This path contains an average grain size of 34 µm with large granular bainite, and martensitic lath packet sizes greater than 60 µm in length. Some M-A, and retained austenite (RA), which is less resistant to dislocation movement, are present, as shown in Fig.13 (a). The X2 path possesses better fracture resistance as a result of the crack following the annealed and soft zone between the two layer bands. This region is refined with average grain sizes of 24 µm with fine grain bainite and quasi polygonal ferrite, as shown in Fig. 13 (b), hence the improved toughness. In both cases subgrain sizes < 1 µm are present. The preferential fracture path in the X direction would have been the hard region (X1 path) as claimed in the work of [33] if there were no side grooving.

4.4 The influence of microstructure, inclusion, and precipitates on fracture toughness

The fractured morphologies of the J_{IC} specimens analysed with EDS, showing the inclusions and particles found in the fractured zone, are shown in Fig. 14 (a - f). As a result of heating and relatively slow cooling of the

Journal Pre-proof

WAAM OS structure, there is a fine distribution of carbides, oxides and intermetallic compounds in the ferrite matrix. The presence of mainly fine non-equiaxed ferrite of an interwoven (basket weave) nature, called AF, was found in the ER70S-6 WAAM deposit, as shown in Fig. 8 (f). The interlocking nature of acicular ferrite, plus its fine grains, promotes maximum fracture resistance, hence the maximum J_q value of $640kj/m^2$. The Ti and Mn oxide inclusion in this steel deposit, as revealed by EDS scanning in Fig.14 (a & b), contributed to the intragranular transformation of titanium and manganese rich amorphous phases, with Mo delaying and suppressing the formation of PF and P and promoting AF; this is consonant with the work of [15]. The work of [39] also revealed that Ti non metallic inclusions in welds support AF formation due to the replacement of $MnSiO_3$ by Mn_2TiO_4 and $MnTiO_3$ and finally Ti_2O_3 with some effectively depleted manganese (Mn) zones. In Fig. 14 (a & b), the high triaxial state stress was reflected in the high plasticity possessed by the ER70S-6 WAAM deposit; this was shown in the copious, equiaxed shaped, small deep and closer dimples in the fractured surface. Hence, the decrease in dimple size as energy per unit area required to fracture increases. The Z path specimen had more and smaller dimples. The fracture mechanism is caused by ductile failure and the smaller sized dimples depict its high ductility, hence the tougher it was compared to other WAAM OS deposited steels.

The microstructure presented by the ER90S-B3 is more coarsening, as shown in Fig. 8 (b). It contains M-A constituent consisting of martensitic laths, upper bainite, and GBF. These hard phases are promoted by the presence of a high volume of Cr and Mo, as shown in Table 1. The formation of grain boundary ferrite and upper bainite provides an easy pathway for crack propagation, hence, the lowest J_q value of $350kj/m^2$ compared to ER70S-6 & ER120S-G. Fine spherical carbide precipitates of Fe_3C, Mo_2C and inclusions of AlO, MnS, Al-Si were observed in the fractured surface as shown in Fig. 14 (c & d). It was also reported by [40] that the non uniform micro straining of the matrix and dislocation locking caused by these precipitates are responsible for the fracture behaviour of these steels. According to [41], $M_{23}C_6$ and M_7C_6 are the secondary precipitates found in the weld subzone that weaken the fracture path and lead to micro void generation. The large sized non equiaxed intragranular dimples were as a result of the weak influence of the microstructure on the fracture behaviour. The dimple sizes in the Z and X paths are similar. The fracture mechanism is through micro-void coalescence with some quasi cleavage and dimple fracture.

The fracture surface of WAAM ER120S-G revealed the presence of Ti, Al and Mn inclusions, as shown in Fig. 14 (e & f). The reduced inclusion number, as a result of aluminium retarding ferrite transformation, leads to the presence of a low amount of AF [42–44]. Precipitation and homogeneously dispersed carbides and oxides in

Journal Pre-proof

the ferrite matrix were responsible for the improvement in strength and toughness of the WAAM ER120S-G steel. The fine inclusion particles act as nucleation sites for acicular ferrite formation [45]. This also has huge effects on grain boundary pinning, hence the reduced average grain size of < 12µm and sub grains of < 1µm. The micro constituents form interlocking structures in the microstructure that improves strength and toughness [45–47]. The combined presence of Ni (2.27%) and Mo (0.63%) in certain proportions in the original chemistry of the wire aided the reduction of both second phase and GBF, hence the high $\boldsymbol{J_q}$ value of *400*kj/m^2. This is consonant with [28]. The presence of numerous large equiaxed dimples reflect the ductility attributes of this steel. WAAM of steel is a constructive process and it enhances displacive transformation regimes in the steel making process. Intragranular ferrite formed at a displacive transformation temperature is a dominant feature of the acicular ferrite in the deposited metal. The kinetics of ferrite nucleation and growth reaction at the austenite grain boundary and intragranular nucleation sites determine the extent of acicular ferrite formation. The fracture toughness of low alloy steel is dependent on the volume fraction of AF. Austenite grain size, alloy content and inclusion characteristics with WAAM deposition parameters are the factors controlling the large volume fraction of AF in WAAM steel deposits.

Journal Pre-proof

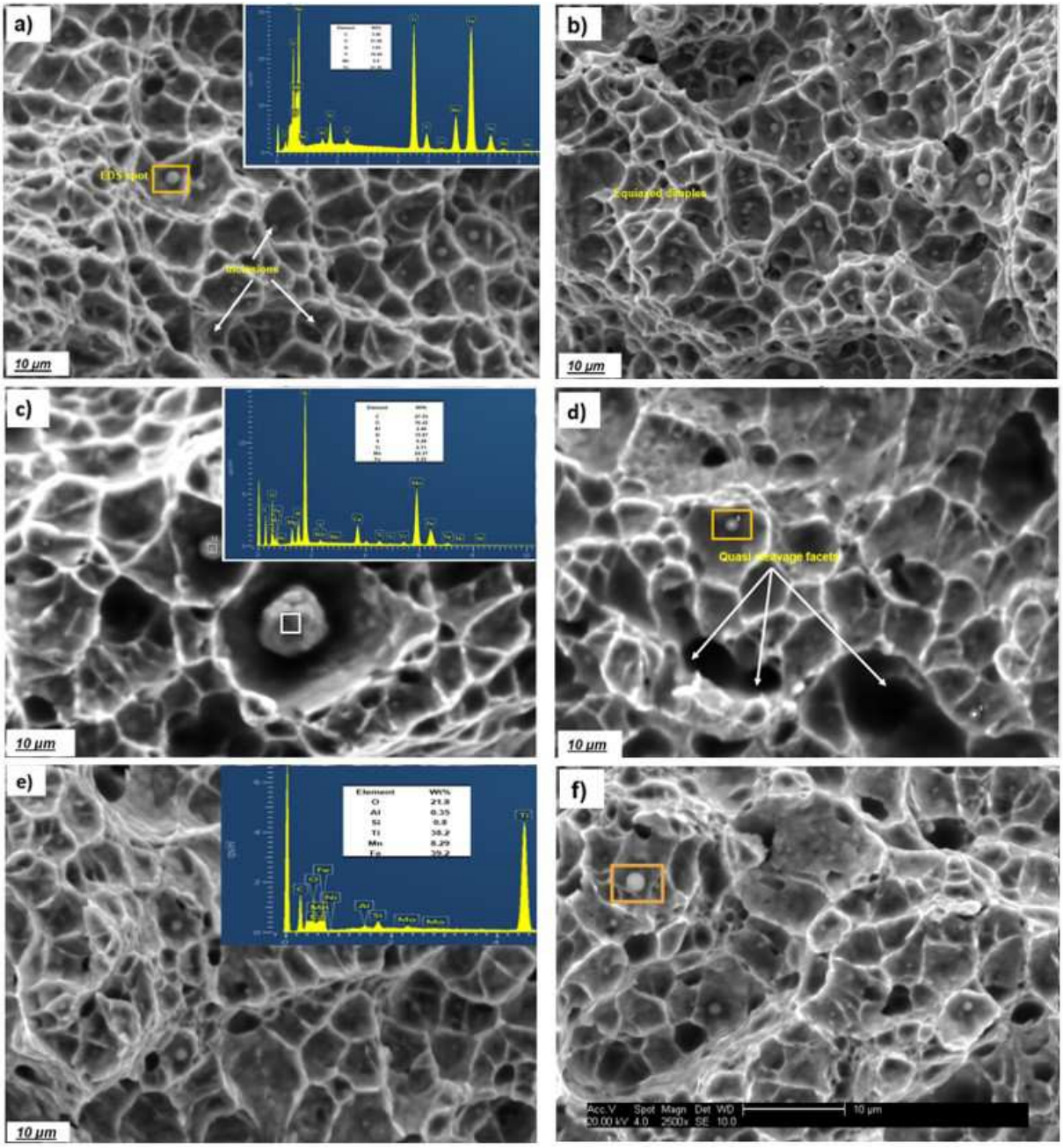


Fig. 14 : Fracture morphologies for *J1*C specimen in both X & Z direction with EDS analysis of round particles (a) ER70S-6(Z) (b) ER70S-6(X) (c) 90S-B(Z) (d) 90S-B (X) (e) ER120S-G (Z) (f) ER120S-G (X)

5. Conclusions

In this paper, the WAAM OS and SP deposition strategy was used to deposit HSLA steel structures. The metallurgical structure, the basic mechanical properties, and the fracture toughness in terms of $\mathbf{J_{IC}}$ values of the WAAM OS deposit in different orientations were experimentally determined using the EPFM approach. The following conclusions are drawn from the studies:

Journal Pre-proof

- The cause of variability in J_q in the WAAM OS strategy deposits is the hardening and softening regions in the layer bands caused by the variation in peak temperature and cooling rates of the adjacent layer in the building direction.

- The fracture toughness J_q across the Z-direction possesses the most resistance to fracture failure as a result of the reduced grain sizes due to grain refinement and increased density of grain boundaries in the Z-direction.

- The fracture toughness J_q along the welding direction possesses the least resistance to fracture failure as a result of increased grain size in the welding direction and the tendency for crack propagation in the most vulnerable part in the microstructure, i.e. hardened zone in the layer band.

- The dominating mechanism of failure in the WAAM oscillated steel is ductile fracture, bound with large and small dimples, and with some fine dispersed carbides and oxides in the ferrite matrix.

- WAAM built by oscillatory strategy is a constructive process for producing HSLA steel structures since it enhances displacive transformation regimes with a unique microstructure.

- The layer band spacing and the thickness of the hard zone are key parameters that could control the fracture toughness of WAAM oscillated part in the Z-directions, this require to be further investigated.

- Fracture toughness behaviour of WAAM steels made by single pass and parallel pass strategies will be investigated further.

Acknowledgements: The authors acknowledge the funding from the European Union's HORIZON 2020 research and innovation programme under grant agreement No. 723600. The authors also acknowledge the support of Vestas wind system A/S and Total E & P Nigeria Limited (TEPNG) for their financial support.

Conflicts of Interest: The authors declare no conflict of interest.

References

[1] H. Roedter, M. Gagné, Ductile Iron for Heavy Section Wind Mill Castings: An European Experience,

Journal Pre-proof

Keith Millis Symp. Ductile Iron. 1 (2003). http://www.ductile.org/Magazine/2005_2/windmill.pdf.

[2] The Crown Estate, Offshore Wind - Operational report 2016, The Crown Estate. (2016). doi:10.1016/B978-0-12-410422-8.00003-0.

[3] M. Shirani, G. Härkegård, Large scale axial fatigue testing of ductile cast iron for heavy section wind turbine components, Eng. Fail. Anal. 18 (2011) 1496–1510. doi:10.1016/j.engfailanal.2011.05.005.

[4] M. Shirani, G. Härkegård, Fatigue life distribution and size effect in ductile cast iron for wind turbine components, Eng. Fail. Anal. 18 (2011) 12–24. doi:10.1016/j.engfailanal.2010.07.001.

[5] J. Patel, S. Jansto, Niobium high strength steels for greener wind power generation, Millenium Steel. (2012) 171–175.

[6] R. Schnitzer, D. Zügner, P. Haslberger, W. Ernst, E. Kozeschnik, Influence of alloying elements on the mechanical properties of high-strength weld metal, Sci. Technol. Weld. Join. 22 (2017) 536–543. doi:10.1080/13621718.2016.1274095.

[7] N.J. Kim, The Physical Metallurgy of HSLA Linepipe Steels—A Review, JOM J. Miner. Met. Mater. Soc. 35 (1983) 21–27. doi:10.1007/BF03338239.

[8] L.F. Porter, P.E. Repas, The Evolution of HSLA Steels, JOM J. Miner. Met. Mater. Soc. 34 (1982) 14–21. doi:10.1007/BF03337994.

[9] T. Koseki, S. Ohkita, N. Yurioka, Thermodynamic study of inclusion formation in low alloy steel weld metals, Sci. Technol. Weld. Join. 2 (1997) 65–69. doi:10.1179/stw.1997.2.2.65.

[10] Z. Tang, W. Stumpf, The role of molybdenum additions and prior deformation on acicular ferrite formation in microalloyed Nb-Ti low-carbon line-pipe steels, Mater. Charact. 59 (2008) 717–728. doi:10.1016/j.matchar.2007.06.001.

[11] J.R. Yang, C.Y. Huang, C.F. Huang, J.N. Aoh, Influence of acicular ferrite and bainite microstructures on toughness for an ultra-low-carbon alloy steel weld metal, J. Mater. Sci. Lett. 12 (1993) 1290–1293. doi:10.1007/BF00506341.

[12] D. V. Edmonds, R.C. Cochrane, Structure-property relationships in bainitic steels, Metall. Trans. A. 21 (1990) 1527–1540. doi:10.1007/BF02672567.

Journal Pre-proof

[13] W.L. Costin, O. Lavigne, A. Kotousov, A study on the relationship between microstructure and mechanical properties of acicular ferrite and upper bainite, Mater. Sci. Eng. A. 663 (2016) 193–203. doi:10.1016/j.msea.2016.03.103.

[14] N. Sridharan, M.W. Noakes, A. Nycz, L.J. Love, R.R. Dehoff, S.S. Babu, On the toughness scatter in low alloy C-Mn steel samples fabricated using wire arc additive manufacturing, Mater. Sci. Eng. A. 713 (2018) 18–27. doi:10.1016/j.msea.2017.11.101.

[15] M. Fattahi, N. Nabhani, M. Hosseini, N. Arabian, E. Rahimi, Effect of Ti-containing inclusions on the nucleation of acicular ferrite and mechanical properties of multipass weld mFattahi, M., Nabhani, N., Hosseini, M., Arabian, N., & Rahimi, E. (2013). Effect of Ti-containing inclusions on the nucleation of acicula, Micron. 45 (2013) 107–14. doi:10.1016/j.micron.2012.11.004.

[16] S.S. Babu, In pursuit of optimum welding system design for steels, Sci. Technol. Weld. Join. 16 (2011) 306–312. doi:10.1179/1362171811Y.0000000019.

[17] M.C. Zhao, K. Yang, Y. Shan, The effects of thermo-mechanical control process on microstructures and mechanical properties of a commercial pipeline steel, Mater. Sci. Eng. A. 335 (2002) 14–20. doi:10.1016/S0921-5093(01)01904-9.

[18] Y. Zhong, F. Xiao, J. Zhang, Y. Shan, W. Wang, K. Yang, In situ TEM study of the effect of M/A films at grain boundaries on crack propagation in an ultra-fine acicular ferrite pipeline steel, Acta Mater. 54 (2006) 435–443. doi:10.1016/j.actamat.2005.09.015.

[19] X. Xu, S. Ganguly, J. Ding, S. Guo, S. Williams, F. Martina, Microstructural evolution and mechanical properties of maraging steel produced by wire + arc additive manufacture process, Mater. Charact. 143 (2018) 152–162. doi:10.1016/j.matchar.2017.12.002.

[20] X. Xu, S. Ganguly, J. Ding, P. Dirisu, F. Martina, X. Liu, S.W. Williams, Improving mechanical properties of wire plus arc additively manufactured maraging steel through plastic deformation enhanced aging response, Mater. Sci. Eng. A. 747 (2019). doi:10.1016/j.msea.2018.12.114.

[21] A. Caballero, J. Ding, S. Ganguly, S. Williams, Wire + Arc Additive Manufacture of 17-4 PH stainless steel: Effect of different processing conditions on microstructure, hardness, and tensile strength, J. Mater. Process. Technol. 268 (2019) 54–62. doi:10.1016/j.jmatprotec.2019.01.007.

Journal Pre-proof

[22] A. Ho, H. Zhao, J.W. Fellowes, F. Martina, A.E. Davis, P.B. Prangnell, Acta Materialia On the origin of microstructural banding in Ti-6Al4V wire-arc based high deposition rate additive manufacturing, Acta Mater. 166 (2019) 306–323. doi:10.1016/j.actamat.2018.12.038.

[23] C. V. Haden, G. Zeng, F.M. Carter, C. Ruhl, B.A. Krick, D.G. Harlow, Wire and arc additive manufactured steel: Tensile and wear properties, Addit. Manuf. 16 (2017) 115–123. doi:10.1016/j.addma.2017.05.010.

[24] T.A. Rodrigues, V. Duarte, J.A. Avila, T.G. Santos, R.M. Miranda, J.P. Oliveira, Wire and arc additive manufacturing of HSLA steel: Effect of thermal cycles on microstructure and mechanical properties, Addit. Manuf. 27 (2019) 440–450. doi:10.1016/j.addma.2019.03.029.

[25] J. Chen, Y. Verreman, J. Lanteigne, On fracture toughness J IC testing of martensitic stainless steels, (2013) 1–9.

[26] J.H. Underwood, JIc Test Results From Two Steels, Astm Stp 601. (1976) 312–329.

[27] A. Elrefaey, Effectiveness of cold metal transfer process for welding 7075 aluminium alloys, Sci. Technol. Weld. Join. 20 (2015) 280–285. doi:10.1179/1362171815Y.0000000017.

[28] S.D. Bhole, J.B. Nemade, L. Collins, C. Liu, Effect of nickel and molybdenum additions on weld metal toughness in a submerged arc welded HSLA line-pipe steel, Material. 173 (2006) 92–100. doi:10.1016/j.jmatprotec.2005.10.028.

[29] N.C. Law, D. V Edmonds, The formation of austenite in a low alloy steel, Metall. Mater. Ransactions. 11A (1980) 33–46.

[30] K. Sindo, Welding Metallurgy, 2nd ed., John Wiley and Sons, United States of America, 2003.

[31] A. Lambert-Perlade, A.F. Gourgues, J. Besson, T. Sturel, A. Pineau, Mechanisms and modeling of cleavage fracture in simulated heat-affected zone microstructures of a high-strength low alloy steel, Metall. Mater. Trans. A Phys. Metall. Mater. Sci. 35 (2004) 1039–1053. doi:10.1007/s11661-004-1007-6.

[32] S.S. Babu, The mechanism of acicular ferrite in weld deposits, Curr. Opin. Solid State Mater. Sci. 8 (2004) 267–278. doi:10.1016/j.cossms.2004.10.001.

[33] X. Zhang, F. Martina, J. Ding, X. Wang, S.W. Williams, Fracture toughness and fatigue crack growth

Journal Pre-proof

rate properties in wire + arc additive manufactured Ti-6Al-4V, Fatigue Fract. Eng. Mater. Struct. 40 (2017) 790–803. doi:10.1111/ffe.12547.

[34] F. Martina, P.A. Colegrove, S.W. Williams, J. Meyer, Microstructure of Interpass Rolled Wire + Arc Additive Manufacturing Ti-6Al-4V Components, Metall. Mater. Trans. A. 46 (2015) 6103–6118. doi:10.1007/s11661-015-3172-1.

[35] M. Lomozik, Effect of the welding thermal cycles on the structural changes in the heat affected zone and on its properfies in joints welded in low-alloy steels, Weld. Int. 14 (2000) 845–850. doi:10.1080/09507110009549281.

[36] I. Yadroitsev, P. Krakhmalev, I. Yadroitsava, S. Johansson, I. Smurov, Energy input effect on morphology and microstructure of selective laser melting single track from metallic powder, J. Mater. Process. Technol. 213 (2013) 606–613. doi:10.1016/j.jmatprotec.2012.11.014.

[37] J.D.Hunt, Steady state columnar and equiaxed growth of dendrites and eutectic, Mater. Sci. Eng. 65 (1984) 75–83. doi:10.1016/0025-5416(84)90201-5.

[38] J. Ge, J. Lin, Y. Chen, Y. Lei, H. Fu, Characterization of wire arc additive manufacturing 2Cr13 part: Process stability, microstructural evolution, and tensile properties, J. Alloys Compd. 748 (2018) 911–921. doi:10.1016/j.jallcom.2018.03.222.

[39] J. Byun, J. Shim, Y.W. Cho, D.N. Lee, Non-metallic inclusion and intragranular nucleation of ferrite in Ti-killed C – Mn steel, Acta Mater. 51 (2003) 1593–1606. doi:10.1016/S1359-6454(02)00560-8.

[40] R.. Swift, Embrittlement of 2-1/4Cr-1Mo Steel Weld Metal by Postweld Heat Treatment, Weld. Res. Suppl. (1973) 145–153.

[41] R.K.S. Raman, Influence of Microstructural Variations in the Weldment on the High-Temperature Corrosion of 2 . 25Cr-1Mo Steel, Metall. Mater. Trans. A. 26 (1995).

[42] T. Yamada, H. Terasaki, Y. Komizo, Relation between Inclusion Surface and Acicular Ferrite in Low Carbon Low Alloy Steel Weld, ISIJ Int. 49 (2009) 1059–1062. doi:10.2355/isijinternational.49.1059.

[43] D.S. Sarma, A. V. Karasev, P.G. Jönsson, On the Role of Non-metallic Inclusions in the Nucleation of Acicular Ferrite in Steels, ISIJ Int. 49 (2009) 1063–1074. doi:10.2355/isijinternational.49.1063.

Journal Pre-proof

[44] A.M. Paniagua-Mercado, V.M. Lopez-Hirata, H.J. Dorantes-Rosales, P. Estrada Diaz, E. Diaz Valdez, Effect of TiO2-containing fluxes on the mechanical properties and microstructure in submerged-arc weld steels, Mater. Charact. 60 (2009) 36–39. doi:10.1016/j.matchar.2008.06.003.

[45] S. Kou, Welding metallurgy, 2nd ed., Wiley, Hoboken, NJ, 2003.

[46] Y. Kang, J. Jang, J.H. Park, C. Lee, Influence of Ti on non-metallic inclusion formation and acicular ferrite nucleation in high-strength low-alloy steel weld metals, Met. Mater. Int. 20 (2014) 119–127. doi:10.1007/s12540-014-1013-1.

[47] J. Zachrisson, J. Borjesson, L. Karlsson, Role of inclusions in formation of high strength steel weld metal microstructures, Sci. Technol. Weld. Join. 18 (2013) 603–609. doi:10.1179/1362171813Y.0000000138.

Journal Pre-proof

Journal Pre-proof

List of Figures

Fig. 1. (a) WAAM oscillatory pass strategy (b) Single pass strategy (c) WAAM built (d) J_{IC} fracture toughness testing

Fig. 2. (a) Oscillatory deposited wall geometry with C(T) machining matrix (b) tensile cut specimen (c) tensile specimens machining matrix

Fig. 3. (a) C(T) specimen dimensioned as per ASTM E1820 (b) side grooved C(T) specimen geometry

Fig. 4. J_{IC} Fracture testing (a) across the layer (Z-direction sample) (b) along the layers (X-direction sample (X2)) (c) along the layers (X-direction sample (X1))

Fig. 5. The average value of strength vs. elongation for both strategies

Fig. 6. The stress-strain curve obtained in Oscillatory strategy

Fig. 7. Hardness variation in WAAM oscillated strategy

Fig. 8. Optical micrographs of single pass deposition (a) ER70S-6 (b) ER90S-B3 (c) ER120S-G, Oscillatory pass deposition with SEM image in picture (d) ER70S-6 (e) ER90S-B3 (f) ER120S-G

Fig. 9. WAAM deposited structure of (ER90S-B3) (a) loading and unloading curve (b) J-R

Fig. 10 J_{IC} plot (a) illustration of the exclusion lines and J_{max} & J_{IC} (b) J_q Values for the different fracture orientation in WAAM deposited steel components.

Fig. 11. Macro image showing layer bands and fractured, cracked path in WAAM deposited steel component

Fig. 12. Macro of fractured CT specimen in both direction (a) Z-direction (CT) (b) fractured area (5mm) (c) X-dir. (CT) (d) fractured area (5mm)

Fig. 13. SEM details microstructural features of 90S-B3 WAAM deposited features with fine distribution of carbides (a) X1 fracture path (b) X2 fracture

Fig. 14 : Fracture morphologies for J1C specimen in both X & Z direction with EDS analysis of round particles (a) ER70S-6(Z) (b) ER70S-6(X) (c) 90S-B(Z) (d) 90S-B (X) (e) ER120S-G (Z) (f) ER120S-G (X)

List of Tables

Table 1. Chemical Composition (%wt) of Wires

Table 2. Summary of fracture toughness test results

Journal Pre-proof

Journal Pre-proof



https://dspace.org/

Analysis of fracture toughness properties of wire + arc additive manufactured high strength low alloy structural steel components

Dirisu, Philip; Ganguly, Supriyo; Mehmanparast, Ali; Martina, Filomeno; Williams, Stewart W.

2020-08-14
Elsevier
https://doi.org/10.1016/j.msea.2019.138285
Dirisu P, Ganguly S, Mehmanparast A, et al., (2019) Analysis of fracture toughness properties of wire + arc additive manufactured high strength low alloy structural steel components. Materials Science and Engineering A: Structural Materials: Properties, Microstructures and Processing, Volume 765, September 2019, Article number 138285

Downloaded from a DSpace repository. https://dspace.org/